

# Divalent Metal Cations Stimulate Skeleton Interoception to Promote Bone Formation

Xu Cao (✉ [xcao11@jhmi.edu](mailto:xcao11@jhmi.edu))

Johns Hopkins University <https://orcid.org/0000-0001-8614-6059>

Wei Qiao

The University of Hong Kong

Dayu Pan

Johns Hopkins school of Medicine

Yufeng Zheng

Peking University <https://orcid.org/0000-0002-7402-9979>

Shuilin Wu

Tianjin University

Xuanyong Liu

Chinese Academy of Sciences

Zhuofan Chen

Sun Yat-sen University <https://orcid.org/0000-0002-3341-1485>

Mei Wan

Johns Hopkins University <https://orcid.org/0000-0001-9404-540X>

Shiqing Feng

Tianjin Medical University General Hospital Qilu Hospital <https://orcid.org/0000-0001-7913-5773>

Kenneth Cheung

University of Hong Kong

Kelvin Yeung

The University of Hong Kong <https://orcid.org/0000-0003-0887-088X>

---

## Article

**Keywords:** divalent metal cations, prostaglandin E2, EP4

**Posted Date:** August 9th, 2021

**DOI:** <https://doi.org/10.21203/rs.3.rs-745307/v1>

**License:**   This work is licensed under a Creative Commons Attribution 4.0 International License.

[Read Full License](#)

**Version of Record:** A version of this preprint was published at Nature Communications on January 27th, 2022. See the published version at <https://doi.org/10.1038/s41467-022-28203-0>.

# Abstract

Bone formation induced by divalent metal cations has been widely reported; however, the underlying mechanism is unclear. Here we report that these cations stimulate skeleton interoception by promoting prostaglandin E<sub>2</sub> (PGE<sub>2</sub>) secretion from macrophages. This immune response is accompanied by the sprouting and arborization of calcitonin gene-related polypeptide- $\alpha^+$  nerve fibers, which sense the inflammatory cue with PGE<sub>2</sub> receptor 4 (EP4) and convey the interoceptive signals to the central nervous system. Activating skeleton interoception downregulates sympathetic tone for new bone formation. Moreover, either macrophage depletion or knockout of cyclooxygenase-2 in the macrophage abolishes divalent cation-induced skeleton interoception. Furthermore, sensory denervation or knockout of EP4 in the sensory nerves eliminates the osteogenic effects of divalent cations. Thus, our study reveals that divalent cations promote bone formation through the skeleton interoception circuit, a finding which could prompt the development of novel biomaterials to elicit the therapeutic power of these divalent cations.

## Introduction

Various divalent metal cations have been known to induce new bone formation<sup>1-6</sup>. However, it remains unclear whether the central nervous system (CNS), which has emerged to play an important role in bone homeostasis<sup>7-10</sup>, is involved in this process. The CNS not only reacts to external stimuli, such as temperature, sound, odor, and taste, as exteroception but also receives signals from many physiological systems inside the body, including the cardiovascular, respiratory, gastrointestinal, genitourinary systems, and nociceptive systems, as interoception. In recent years, the interoceptive processes by which our body senses, interprets, integrates, and regulate signals from peripheral organs has emerged as a key mechanism for the control of internal state of our body by CNS<sup>11</sup>. The interoception system consists of ascending neural pathways that transmit the internal body signals to the brain, the CNS where the input interoceptive information is processed, and the descending neural pathways through which the interoceptive signals are circled back to regulate peripheral organs. In addition to the central and peripheral nervous system, several other components, such as the endocrine and immune systems, are proposed to be involved in the interoception process<sup>12,13</sup>.

Unmyelinated free sensory nerve endings branch throughout tissues to recognize and carry signals related to pain, temperature, and mechanical stimuli<sup>14</sup>. As the largest organ, the skeleton accounts for more than 20% of human body weight. Bone tissues have abundant sensory and sympathetic innervations that connect bones with dorsal root ganglia (DRG) and the CNS<sup>15-17</sup>. The upregulation of sympathetic tone through serotonin and cAMP-response element binding protein (CREB) signaling in the hypothalamus contributes to decreased bone formation and increased bone resorption<sup>9,18</sup>. We have recently found that CNS senses bone density through prostaglandin E<sub>2</sub> (PGE<sub>2</sub>) as an ascending interoceptive signal and regulate bone formation through sympathetic nerves as the descending interoceptive pathway<sup>10</sup>. Specifically, PGE<sub>2</sub> secreted by osteoblasts in response to mechanical loading activates PGE<sub>2</sub> receptor4 (EP4) to stimulate phosphorylation of CREB in hypothalamus, where the

tyrosine hydroxylase (TH) expression is downregulated for sympathetic activity to induce commitment of mesenchymal stem/stromal cell (MSCs) to osteoblast lineage. Knockout of the *EP4* gene in the sensory nerves or knockout of cyclooxygenase-2 (COX2) in the osteoblastic cells significantly increased sympathetic activity and reduced bone volume in adult mice. Our most recent studies further demonstrate that ascending skeleton interoceptive signaling target hypothalamus to maintain the balance between bone and fat metabolism<sup>19,20</sup>. Moreover, we also showed sensory innervation into porous endplates is responsible for spinal hypersensitivity, thus, low-dose celecoxib maintains skeleton interoception in the endplate, thereby decreasing vertebral endplate porosity and innervation for the treatment of spinal pain<sup>21,22</sup>. Therefore, the skeleton interoception could represent essential circuit of the CNS in the control of bone metabolism and may shed a light on our understanding of divalent metal cation-induced bone formation.

Innate and adaptive immune processes, which become profoundly apparent after bone injury, play important roles in bone biology<sup>23</sup>. The presence of a series of immune cell-derived cytokines in the early inflammatory stage promote the recruitment of fibroblasts, mesenchymal stem cells, and osteoprogenitor cells from their local niches to initiate bone repair<sup>24,25</sup>. For example, PGE<sub>2</sub>, a well-recognized pro-inflammatory cytokine that is upregulated only during the initial stage of bone healing, is suggested to play an important role in new bone formation. The mutation of the 15-hydroxyprostaglandin dehydrogenase gene (*HPGD*), which is responsible for the degradation of PGE<sub>2</sub><sup>26</sup>, plays a major role in promoting tissue regeneration<sup>27,28</sup>. Indeed, patients with an *HPGD* mutation have presented with subperiosteal new bone formation<sup>29</sup>. Since PGE<sub>2</sub> can elicit primary pain and prolong nociceptor sensitization<sup>30,31</sup>, nonsteroidal anti-inflammatory drugs (NSAIDs), which inhibit cyclooxygenase (COX), the limiting enzyme of PGE<sub>2</sub>, have been used to manage post-injury pain. However, there is increasing evidence that the use of NSAIDs, especially selective COX2 inhibitors, can affect bone healing<sup>32,33</sup>. These findings suggest that the inflammatory molecules produced by the immune system in response to bone injury may serve as biochemical signals to initiate the interoceptive control of bone regeneration.

In recent years, the immunomodulatory function of orthopedic biomaterials has been increasingly acknowledged. In fact, the host immune response to implanted biomaterials is now better understood for the long-term survival and regenerative function of such biomaterials<sup>34,35</sup>. Divalent metal cations, such as magnesium ions (Mg<sup>2+</sup>), zinc ions (Zn<sup>2+</sup>), and copper ions (Cu<sup>2+</sup>), have been extensively used to modify orthopedic biomaterials since the discovery of their osteogenic effects<sup>5,36-39</sup>. However, despite their well-recognized roles in the regulation of the immune response<sup>40</sup>, the mechanism through which the divalent cation-modulated immune niche contributes to bone regeneration remains largely unclear. Indeed, the *in vitro* effects of divalent metal cations on osteogenesis starkly contradict our findings in a more complex *in vivo* model, because their osteogenic effects on the well-orchestrated bone healing process may involve the interplay of multiple systems in our body. We have recently showed the essential role of early inflammatory response in Mg<sup>2+</sup>-induced new bone formation, as Mg<sup>2+</sup> stimulates macrophage via transient receptor potential cation channel member 7 (TRPM7) to create a pro-

osteogenic immune microenvironment<sup>4</sup>. Since the effective window of Mg<sup>2+</sup> coincides with the reinnervation phase of bone healing<sup>41</sup>, we hypothesize the communication between the immune system and the neural system can trigger the skeleton interoception for the regulation of new bone formation.

In this study, we sought to characterize the mechanism for divalent cation–induced bone formation. We found that divalent metal cations, including Mg<sup>2+</sup>, Zn<sup>2+</sup>, and Cu<sup>2+</sup>, activated skeletal interoception through the immune-neural axis to initiate CNS regulation of bone formation. During the early stage of bone healing, divalent cation–induced PGE<sub>2</sub> secretion from macrophages stimulated EP4 in the sensory nerves. Importantly, the sprouting and arborization of sensory nerves in response to macrophage-derived PGE<sub>2</sub> transmitted interoceptive signals to the CNS to tune down sympathetic tone through hypothalamic CREB signaling, resulting in increased osteogenesis and decreased osteoclastogenesis in the injured bone. We revealed a previously unknown role of divalent cations in bone formation through skeletal interoception.

## Results

### Divalent cation–induced bone formation

To investigate the effect of metallic divalent cations including Mg<sup>2+</sup>, Zn<sup>2+</sup> or Cu<sup>2+</sup> on bone formation, we used an alginate-based hydrogel to facilitate the temporary and localized delivery of these divalent cations in mouse femurs (**Extended data Fig. 1a**) after evaluating their cytotoxicity *in vitro* (**Extended data Fig. 1b**). Pure alginate (Alg) or divalent cation–releasing alginate (i.e., Mg-Alg, Cu-Alg, and Zn-Alg) was placed in a tunnel defect drilled from the patellofemoral groove of the distal femur along the axis of the femoral shaft. Micro-computed tomography (μCT) analysis showed a substantial increase in bone volume fraction (BV/TV), bone mineral density (BMD of TV), and polar moment of inertia (pMOI) in the femur 4 weeks after the placement of divalent cation–releasing alginate compared with the pure alginate-treated control mice (**Fig. 1a, b, Extended data Fig. 2a**). Particularly, cortical bone area (Ct.Ar), cortical bone thickness (Ct.T), and bone perimeter (B.Pm) were greater in the divalent cation–treated group compared with the controls (**Fig. 1a, b, Extended data Fig. 2a**). We found a similar trend in the increase of trabecular thickness (Tb.T) in the femurs treated with Mg<sup>2+</sup> or Cu<sup>2+</sup>, although it was less pronounced (**Extended data Fig. 2a**). Indeed, hematoxylin and eosin (H&E) staining showed significant new bone formation located primarily at the peripheral cortex in the divalent cation–treated femurs (**Fig. 1c**). Moreover, immunofluorescent staining revealed that the number of osteocalcin<sup>+</sup> (OCN<sup>+</sup>) osteoblasts increased significantly on the endocortical and periosteal surfaces of femurs treated with Mg<sup>2+</sup>, Zn<sup>2+</sup>, or Cu<sup>2+</sup> (**Fig. 1d, Extended data Fig. 2b**). Meanwhile, the number of tartrate-resistant acid phosphatase<sup>+</sup> (TRAP<sup>+</sup>) cells on the endocortical and periosteal surfaces decreased significantly in the divalent cation–treated femurs compared with the controls (**Fig. 1e, Extended data Fig. 2b**). In particular, the number of osterix<sup>+</sup> and Runx2<sup>+</sup> osteoprogenitors in the periosteum was also significantly higher after the release of Mg<sup>2+</sup> from the hydrogel (**Extended data Fig. 2c, d**). Therefore, our results reveal that divalent cations, including Mg<sup>2+</sup>, Zn<sup>2+</sup> and Cu<sup>2+</sup>, could stimulate periosteal new bone formation.

## Divalent cation–induced PGE<sub>2</sub> production from macrophages

To examine the mechanism of divalent cation–induced bone formation, we first tested whether macrophages mediated early inflammation response to the stimulation of divalent cations. Using Mg<sup>2+</sup>-releasing hydrogel as an example, we found that Mg<sup>2+</sup>-induced woven bone formation in the periosteum was observed on day 7 using  $\mu$ CT and H&E staining (**Extended data Fig. 3a, b**). Immunostaining showed that cluster of differentiation 68<sup>+</sup> (CD68<sup>+</sup>) macrophages increased significantly in the bone marrow and periosteum of Mg<sup>2+</sup>-treated femurs compared with controls (**Extended data Fig. 3c**). Moreover, the expression of COX2 was also significantly increased (**Extended data Fig. 3d**). Co-immunostaining of COX2 with CD68 demonstrated that COX2 was expressed primarily in CD68<sup>+</sup> macrophages in the periosteum (**Fig. 2a**), and that the stimulation of divalent cations, including Mg<sup>2+</sup>, Zn<sup>2+</sup>, or Cu<sup>2+</sup>, significantly increased expression of COX2 in CD68<sup>+</sup> macrophages in the callus (**Fig. 2a, b**). Indeed, the release of Mg<sup>2+</sup> significantly elevated PGE<sub>2</sub> concentration in bone (**Fig. 2c**) relative to serum PGE<sub>2</sub> (**Fig. 2d**) during the early stage (i.e., week 1), when the injured site was undergoing acute inflammation. To examine the mechanism of divalent cation–induced COX2 expression, we isolated and cultured the primary mouse bone marrow macrophages (BMM) with the divalent cations. Mg<sup>2+</sup>, Zn<sup>2+</sup>, and Cu<sup>2+</sup> all promoted secretion of PGE<sub>2</sub> (**Fig. 2e**). Importantly, when used at a specific level (i.e., 0.1 mM Zn<sup>2+</sup>, 0.1 mM Cu<sup>2+</sup>, or 10 mM Mg<sup>2+</sup>), the divalent cations upregulated prostaglandin E synthase (PTGES) gene expression (**Fig. 2f**) and protein levels of COX2 in the BMM (**Fig. 2g**) without affecting cell viability (**Extended data Fig. 1b**). Furthermore, divalent cations led to the phosphorylation of nuclear factor- $\kappa$ B (NF- $\kappa$ B) p65 and inhibitor of nuclear factor- $\kappa$ B (I $\kappa$ B $\alpha$ ), the key cascade proteins in the NF- $\kappa$ B signaling pathway (**Fig. 2h**). Indeed, Mg<sup>2+</sup> significantly increased the binding of NF- $\kappa$ B p65 to the COX2 gene promoter as shown in chromatin immunoprecipitation (ChIP) assay (**Fig. 2i**). Thus, we showed that divalent cations stimulate the secretion of PGE<sub>2</sub> from macrophages during the inflammation stage of the bone healing process.

## Ablation of COX2 in macrophages eliminates periosteal bone formation

To validate the mechanism *in vivo*, we established an inducible macrophage–depleted mouse model by crossing LysM-Cre mice with iDTR<sup>wt</sup> mice. Macrophage depletion was effectively achieved in iDTR<sub>LysM</sub><sup>+/-</sup> mice by injecting diphtheria toxin (DTX). Macrophage depletion diminished the effect of Mg<sup>2+</sup> on bone healing, as there was no significant difference between the Mg-Alg group and the control group in bone formation on  $\mu$ CT (**Fig. 3a, b, Extended data Fig. 4a**), whereas, Mg<sup>2+</sup>-releasing hydrogel effectively promoted new bone formation after bone injury in LysM-Cre mice, similar to its effect in WT mice. Interestingly, when bone PGE<sub>2</sub> level was elevated with injection of SW03329 (a PGE<sub>2</sub> degradation enzyme inhibitor), the new bone formation in the injured femur improved significantly in both the control group

and the Mg-Alg group (**Fig. 3c, d, Extended data Fig. 4b**). Specifically, new bone formation at the peripheral cortex of the injured femur with injection of SW033291 in the control group was similar in the  $Mg^{2+}$ -treated group on H&E staining (**Fig. 3e**). Moreover, the numbers of OCN<sup>+</sup> osteoblasts and TRAP<sup>+</sup> osteoclasts on the endocortical and periosteal surfaces of femurs were similar regardless of the presence of  $Mg^{2+}$  in the alginate with injection of SW033291 (**Extended data Fig. 4c, d**).

We further generated mice with conditional COX2 knockout in the macrophages ( $COX2_{LysM}^{-/-}$ ) by crossing  $COX2^{wt}$  mice with LysM-Cre mice.  $Mg^{2+}$ -releasing hydrogel failed to induce thickening of cortical bone in injured femurs of  $COX2_{LysM}^{-/-}$  mice compared with  $COX2^{wt}$  mice (**Fig. 3f, g, Extended data Fig. 4e**).  $Mg^{2+}$ -induced new bone formation at the peripheral cortex of femurs in  $COX2^{wt}$  mice was not seen in  $COX2_{LysM}^{-/-}$  mice on H&E staining (**Fig. 3h**). Again, the effect of  $Mg^{2+}$  on OCN<sup>+</sup> osteoblasts and TRAP<sup>+</sup> osteoclasts on both endocortical and periosteal surfaces was diminished in  $COX2_{LysM}^{-/-}$  mice (**Fig. 3i, j**). These data show that COX2 in macrophages is responsible for PGE<sub>2</sub> production for divalent cation-induced bone formation.

### Sensory nerves are essential for divalent cation-induced bone formation

Given that PGE<sub>2</sub> activates EP4 in the sensory nerve to maintain skeletal interoception activity, we examined whether sensory nerves are associated with divalent cation-induced bone formation. Prominent sprouting and arborization of calcitonin gene-related polypeptide- $\alpha^+$  (CGRP<sup>+</sup>) sensory nerve fibers coursing longitudinally over the outer periphery of the reactive callus were observed in immunostaining of periosteum (**Fig. 4a**). The intensity of CGRP<sup>+</sup> nerve fibers in the periosteum was significantly increased with divalent cations (**Fig. 4b**). Importantly, terminal dendrites of CGRP<sup>+</sup> sensory nerves were spatially associated with CD68<sup>+</sup> macrophages in the reactive periosteum (**Fig. 4c**). Moreover, expression of CGRP was significantly increased in the ipsilateral DRG of mice treated with divalent cations (**Fig. 4d, e**). Interestingly, CGRP<sup>+</sup> dendrite sprouting located primarily around COX2<sup>+</sup> macrophages in the periosteum of  $COX2^{wt}$  mice treated with divalent cations was significantly reduced in  $COX2_{LysM}^{-/-}$  mice (**Extended data Fig. 5a**). We then created a sensory denervation mouse model ( $TrkA_{Avil}^{-/-}$ ) by crossing sensory nerve-specific Cre (Advillin-Cre) mice with nerve growth factor receptor tropomyosin receptor kinase A (TrkA) floxed ( $TrkA^{wt}$ ) mice to confirm the essential role of sensory nerve in divalent cation-induced bone formation. Indeed,  $Mg^{2+}$  significantly increased the density of CGRP<sup>+</sup> sensory nerve fibers in the bone marrow cavity and the endocortical and periosteal surfaces of  $TrkA^{wt}$  mice 7 days after surgery, whereas the number of CGRP<sup>+</sup> sensory nerve fibers in  $TrkA_{Avil}^{-/-}$  mice was significantly lower relative to WT mice (**Fig. 4f**). Similarly,  $Mg^{2+}$  stimulated bone formation in  $TrkA^{wt}$  mice, and such effects were eliminated in  $TrkA_{Avil}^{-/-}$  mice (**Fig. 4g, h, Extended data Fig. 5b**). Taken together, divalent cation-induced sensory innervation in injured bone tissue is essential for new bone formation.

## Divalent cations stimulate PGE<sub>2</sub>/EP4 skeleton interoception in downregulation of sympathetic activity

We have shown that PGE<sub>2</sub> activates sensory nerves via EP4 to induce phosphorylation of CREB in the VMH of the hypothalamus as a skeletal interoception pathway<sup>18,42</sup>. We therefore investigated whether local delivery of divalent cations could trigger CREB phosphorylation in the hypothalamus. Immunostaining of brain sections showed that phosphorylation of CREB was significantly increased in the contralateral VMH of mice at 1 week after the delivery of Mg<sup>2+</sup>, Zn<sup>2+</sup>, or Cu<sup>2+</sup> in the injured femurs (**Fig. 5a**). CREB phosphorylation in the hypothalamus with upregulation in 5-hydroxytryptamine receptor 2C (HTR2C) was confirmed by Western blot analysis (**Extended data Fig. 5c, d**). Moreover, using enzyme-linked immunosorbent assay (ELISA), we showed that Mg<sup>2+</sup> significantly reduced epinephrine levels in serum and urine compared with controls, indicating suppression of sympathetic tone in Mg-Alg-injected mice (**Fig. 5b**). To examine whether divalent cation-induced CREB phosphorylation downregulates tyrosine hydroxylase (TH) for sympathetic activity, we performed immunostaining of TH for sympathetic nerves. The density of TH<sup>+</sup> sympathetic nerve fibers on the periosteal surface of divalent cation-treated femurs was significantly less in mice injected with divalent cation-releasing alginate compared with the controls (**Fig. 5c**). In parallel, spontaneous activity of mice, an indicator of sympathetic tone and postoperative pain<sup>22</sup>, was assessed by spontaneous activity wheels. Compared with controls, the release of Mg<sup>2+</sup> contributed to significantly shorter daily distance and duration, as well as lower maximum speed of running-wheel activity at weeks 1 and 4 after surgery (**Fig. 5d**). Finally, we examined the effect of divalent cations on the activation of skeletal interoception in TrkA<sub>Avil</sub><sup>-/-</sup> and COX2<sub>LysM</sub><sup>-/-</sup> mice, as well as their WT littermates. With sensory nerve denervation, the effect of Mg<sup>2+</sup> on phosphorylation of CREB was diminished compared with their WT littermates (**Fig. 5e**). Daily distance and duration of running-wheel activity in TrkA<sub>Avil</sub><sup>-/-</sup> mice were significantly longer than in their WT littermates (TrkA<sup>wt</sup>), whereas such effect of Mg<sup>2+</sup> on decreasing spontaneous activity was abolished in TrkA<sub>Avil</sub><sup>-/-</sup> mice (**Fig. 5f**). Additionally, the increase of hypothalamic CREB phosphorylation triggered by Mg-Alg was abolished in COX2<sub>LysM</sub><sup>-/-</sup> mice (**Fig. 5g**). Similarly, the effect of Mg<sup>2+</sup> on decreasing the daily distance and duration of running-wheel activity was diminished in COX2<sub>LysM</sub><sup>-/-</sup> mice (**Fig. 5h**). Taken together, our data show that divalent cations promote PGE<sub>2</sub> from macrophages to activate skeletal interoception, resulting in downregulation of sympathetic tone and new bone formation.

## Knockout of EP4 in the sensory nerve inhibits divalent cation-induced activation of skeletal interoception

EP4 is the PGE<sub>2</sub> receptor in the skeletal interoception and is known as the primary receptor in bone remodeling and homeostasis<sup>43</sup>. We first prepared conditional medium from Mg<sup>2+</sup>-treated macrophages to test its effect on EP4 expression. EP4 expression in primary DRG neurons was increased more than 10-

fold relative to treatment with  $Mg^{2+}$  alone (**Fig. 6a**). We then generated  $EP4_{Avil}^{-/-}$  mice by crossing Advillin-Cre mice with  $EP4^{wt}$  mice.  $Mg^{2+}$ -induced bone formation was abolished in  $EP4_{Avil}^{-/-}$  mice with induction of EP4 ablation in the sensory nerves, as shown by  $\mu$ CT (**Fig. 6b, c, Extended data Fig. 5e**). We confirmed with H&E staining that the new bone formation induced by  $Mg^{2+}$  at the peripheral cortex was diminished with conditional knockout of EP4 in sensory nerve fibers (**Fig. 6d**). Moreover, the increase of osteoblasts in the periosteum and decrease of osteoclasts were diminished in  $EP4_{Avil}^{-/-}$  mice after postoperative administration of  $Mg^{2+}$  (**Extended data Fig. 6a, b**). Again, as in COX2 ablation mice, the effect of Mg-Alg on the daily distance and duration of running-wheel activity was also abolished in  $EP4_{Avil}^{-/-}$  mice (**Fig. 6e**). Importantly, phosphorylation of CREB in the hypothalamus was not detectable in  $EP4_{Avil}^{-/-}$  mice treated with Mg-Alg, unlike their  $EP4_{Avil}^{-/-}$  littermates (**Fig. 6f**).

To validate the hypothesis that downregulation of sympathetic activity mediates  $Mg^{2+}$ -induced cortical bone thickening, we injected mice with propranolol, a widely used  $\beta$ 2-adrenergic antagonist. Propranolol contributed to significantly more periosteal new bone formation in  $Mg^{2+}$ -Alg-injected femurs compared with the vehicle group, whereas it failed to increase bone formation in Alg-treated femurs relative to the vehicle group (**Fig. 6g, h, Extended data Fig. 6c**). The bone that was newly formed in response to the stimulation of  $Mg^{2+}$  after the administration of propranolol was located primarily at the peripheral cortex, as was previously observed in WT mice (**Fig. 6i**). Moreover, mice injected with propranolol had a shorter duration of running-wheel activity regardless of Alg or Mg-Alg treatment (**Fig. 6j**). Interestingly, the activation of CREB phosphorylation observed in the contralateral VMH was not prominent after the injection of SW033291 (**Extended data Fig. 6d**), suggesting that the local stimulation caused by the  $Mg^{2+}$ -induced release of  $PGE_2$  from macrophages was largely masked by the systematic administration of SW033291. Similarly, the decrease in spontaneous activity caused by Mg-Alg relative to Alg was diminished as the distance and duration of running-wheel activity in Alg treated mice were lower after the injection of SW033291 (**Extended data Fig. 6e**). Therefore, EP4 in the sensory nerves mediates the activation of skeletal interoception to downregulate sympathetic activity, leading to new bone formation in the injured site.

## Discussion

In recent years, rapid progress has been made in the development of novel biodegradable metal implants<sup>44,45</sup>. With controlled degradation kinetics and gradual integration with bone tissue, biodegradable metal implants have been demonstrated to be superior to traditionally used bioinert metal implants for the treatment of musculoskeletal injuries. Particularly, these biodegradable implants can induce new bone formation through the release of various divalent metal cations<sup>44,45</sup>. Moreover, given the promising osteogenic properties of these divalent metal cations, they are also widely used for the modification of various kinds of orthopedic biomaterials<sup>5,37,46</sup>. Indeed, compared with expensive biological therapeutic agents and complex surgical procedures, the intervention using divalent cations appears to be a cost-effective way to achieve bone regeneration. However, it remains largely unclear how

divalent cations induce new bone formation and whether these divalent cation–releasing biomaterials also induce bone formation through similar molecular and cellular mechanisms. In this study, we discovered that the divalent cations,  $Mg^{2+}$ ,  $Zn^{2+}$ , and  $Cu^{2+}$  serves as interoceptive signals to initiate CNS regulation of new bone formation after injury, which suggests the complexity of the underlying mechanism for divalent cation-induced bone regeneration has been greatly underestimated. Therefore, we believe that a clear understanding of the mechanism through which these divalent cations contribute to new bone formation through interoception will greatly benefit the development of novel biomaterials to fully elicit the therapeutic potential of these divalent cations.

The immune system and the nervous system are paramount to sense and respond to changes in our body, as they possess unique qualities that enable them to counter deviations in the internal environment<sup>12</sup>. Upon the delivery of divalent cations, which disrupts the homeostasis in bone microenvironment, the acute immune response contributes to a series of inflammatory chemokines and cytokines that relay information to the nervous system to initiate interoceptive control of bone formation. As a hallmark of inflammatory response after bone injury, COX2/PGE<sub>2</sub> plays a key role in cortical bone repair<sup>29,32,33</sup>. Subcutaneous administration of PGE<sub>2</sub> contributes to new bone formation on the endocortical and periosteal surfaces of ovariectomized and intact rats<sup>47</sup>, whereas global knockout of COX2 almost eliminates of periosteal bone formation during bone healing<sup>48</sup>. In this study, we showed divalent cations, including  $Mg^{2+}$ ,  $Zn^{2+}$ , and  $Cu^{2+}$ , significantly increased PGE<sub>2</sub> production from CD68<sup>+</sup> macrophages in the reactive periosteum. Interestingly, PGE<sub>2</sub> activated EP4 signaling in the CGRP<sup>+</sup> sensory nerve endings as the biochemical interoceptive signal. Moreover, our data showed that the injection of SW03329 elevated PGE<sub>2</sub> concentration in the control group to support cortical bone formation but did not further significantly promote  $Mg^{2+}$ -induced periosteal new bone formation. This implies that PGE<sub>2</sub>-EP4 signaling in skeletal interoception is not entirely concentration-dependent, and there might be a specific window of PGE<sub>2</sub> levels for the activation of the immune–neural axis during bone healing—if so, this warrants further investigation. This observation suggests that secretion of PGE<sub>2</sub> specifically by macrophages stimulates divalent cations -induced bone formation through skeleton interoception.

Although the immunomodulatory effects of divalent cations have been reported, the inflammatory responses induced by these divalent cations don't always produce specific inflammatory cytokines (e.g., PGE<sub>2</sub>) to facilitate new bone formation<sup>49–52</sup>. Instead, the immunomodulatory effects of these divalent cations are highly concentration-dependent and tissue-specific. The bone tissue is the major reservoir for minerals in human body, thus, the inflammation in this microenvironment induced by high levels of divalent cations may initiate the deposition of these trace minerals in hard tissue to alleviate their potential long-term toxicity. Therefore, the storage exogenous divalent cations in newly formed bone tissue could be an effective and efficient strategy to maintain the physiological condition in bone microenvironment. In this study, by utilizing the different cross-linking potential of  $Mg^{2+}$ ,  $Zn^{2+}$ , and  $Cu^{2+}$  on alginate<sup>53</sup>, Mg-Alg, Zn-Alg, and Cu-Alg were designed exquisitely to harness the immunomodulatory

effects of these divalent cations on macrophages. At very low levels (i.e., approximately 0.1 mM),  $Zn^{2+}$  and  $Cu^{2+}$  produced  $PGE_2$  without eliciting cytotoxicity. In comparison, 10 mM of  $Mg^{2+}$ , similar to degradable magnesium-based implants<sup>54</sup>, stimulated the production of  $PGE_2$  by macrophages, leading to new bone formation, though  $Mg^{2+}$  has been recognized as an anti-inflammatory agent due to its suppressive effects on pro-inflammatory molecules<sup>55,56</sup>. The immunomodulatory effects of the divalent cations were also shown manifested by the activation of the NF- $\kappa$ B signaling pathway in BMM. Given that  $Mg^{2+}$  promotes the nuclear translocation of NF- $\kappa$ B p65 in binding to *COX2* promoter, it is anticipated that the NF- $\kappa$ B signaling pathway, which is crucial in inflammation responses<sup>57</sup>, may play a central role in divalent cation-induced regulation of  $PGE_2$ . In particular, by using a primary culture of DRG neurons and the mice with conditional knockout *COX2* in macrophage, we demonstrated that the activation of sensory neurons is actually triggered by the macrophage-mediated inflammatory microenvironment in response to the stimulation of divalent cations. Moreover, the ablation of EP4 in sensory nerves abolished the osteogenic effect of  $Mg^{2+}$  in the periosteum, thus showing that the crosstalk between immune and neural system is essential in skeletal interoception-mediated new bone formation.

The density of sensory and sympathetic fibers in the periosteum remains the highest in the skeletal system<sup>17</sup>. The periosteum covers almost the entire bone surface and is one of the most regenerative tissues for skeletal osteogenesis<sup>58</sup>. Damage of the periosteum severely impairs cortical bone homeostasis<sup>59,60</sup> and bone fracture healing<sup>44,60</sup>. Moreover, an increase in the density of sensory and sympathetic nerve fibers in injured bone tissue has been reported to contribute to the bone healing process<sup>41,61,62</sup>. CGRP<sup>+</sup> sensory nerves that emanate from the DRG of the spinal cord detect multiple stimuli in bone tissues (including inflammatory cytokines) and process and relay these signals to higher CNS levels<sup>63</sup>. The sprouting and arborization of sensory nerve fibers in the periosteum in response to bone injury<sup>41</sup> or mechanical stimulation<sup>64</sup> may facilitate the sensation of stimuli and the initiation of osteogenesis. Sensory nerve has been found to mediate bone formation with Mg-based metal implants<sup>44</sup>. In our study, a conspicuous increase in the number of CGRP<sup>+</sup> nerve fibers in divalent cation-treated femurs suggests an association between the activation of sensory afferents and the inflammatory microenvironment. Instead of being a local inducer for osteogenic differentiation of bone-forming cells, it is more likely that CGRP, which mainly serves as a neurotransmitter, represents the activation of sensory neurons. The spiral-like TH<sup>+</sup> sympathetic nerve fibers typically wrap around the major blood vessels in the periosteum and penetrate the cortical bone via Volkmann's and Haversian canals<sup>65,66</sup>. They are known to be capable of regulating osteoblast activity through  $\beta$ 2-adrenergic receptors ( $\beta$ 2AR)<sup>9,67</sup>. Meanwhile, by increasing the secretion of the receptor activator of nuclear factor kappa-B ligand (Rankl) from osteoblasts, the sympathetic nervous system can also stimulate osteoclastic bone resorption<sup>8,68</sup>. We found that  $PGE_2$  produced by divalent cation-stimulated macrophages tunes down sympathetic activity for the differentiation of OCN<sup>+</sup> osteoblasts on the endocortical and periosteal surfaces. Moreover, in both the macrophage depletion and sensory denervation models, elevated  $PGE_2$  in the periosteum failed to trigger the activation of CREB signaling in the VMH or periosteal new bone formation, indicating that the

macrophage-mediated immune response and the sensation of afferent nerves are indispensable in the CNS recognition of stimulation from  $Mg^{2+}$ ,  $Zn^{2+}$ , or  $Cu^{2+}$  after bone injury. Importantly, CREB signaling in the ipsilateral DRG and the contralateral VMH by periosteal delivery of divalent cations downregulates sympathetic activity as a precise temporal-spatial feedback to the injured site for bone regeneration.

In summary, we found that skeletal interoception mediates divalent cation–induced bone formation (Fig. 6K). The controlled delivery of  $Mg^{2+}$ ,  $Zn^{2+}$ , or  $Cu^{2+}$  stimulates to the production of  $PGE_2$  from  $CD68^+$  macrophages, which is followed by rapid reinnervation of  $CGRP^+$  sensory nerve fibers in the reactive periosteum. Activation of EP4 receptor in sensory nerves by local  $PGE_2$  induces CREB signaling in the VMH as an ascending interoceptive signal, which downregulates sympathetic activity as a descending interoceptive signal to induce osteogenesis at the injured bone treated with divalent cations. The discovery of divalent cation–induced bone formation through skeletal interoception could revolutionize current understanding of bone regeneration and inspire innovative orthopedic biomaterials for bone tissue engineering.

## Methods

### Mouse breeding

The *Advillin-Cre (Avil-Cre)* mouse strain was kindly provided by Xingzhong Dong (Department of Neuroscience, The Johns Hopkins University, Baltimore, MD, USA). The *TrkA<sup>fl/fl</sup>* mice were obtained from David D. Ginty (Department of Neurobiology, Harvard Medical School, Boston, MD, USA). The *LysM-Cre* mice and *iDTR<sup>fl/fl</sup>* mice were purchased from the Jackson Laboratory (Bar Harbor, ME, USA). The *COX2<sup>fl/fl</sup>* mice were provided by Harvey Herschman (Department of Biological Chemistry, University of California, Los Angeles, Los Angeles, CA, USA). The *EP4<sup>fl/fl</sup>* mice were obtained from Brian L. Kelsall (Laboratory of Molecular Immunology, National Institutes of Health, Bethesda, MD, USA). Heterozygous male *Avil-Cre* mice were crossed with a *TrkA<sup>fl/fl</sup>* or *EP4<sup>fl/fl</sup>* mouse. The offspring were intercrossed to generate the following genotypes: wild type (referred to as WT in the text), *Avil-Cre* (Cre recombinase expressed driven by advillin promoter), *TrkA<sup>fl/fl</sup>* (mice homozygous for TrkA flox allele, referred to as  $TrkA^{wt}$  in the text), *EP4<sup>fl/fl</sup>* (mice homozygous for EP4 flox allele, referred to as  $EP4^{wt}$  in the text), *Avil-Cre::TrkA<sup>fl/fl</sup>* (conditional deletion of TrkA receptor in Advillin lineage cells, referred to as  $TrkA_{Avil}^{-/-}$  in the text), *Avil-Cre::EP4<sup>fl/fl</sup>* (conditional deletion of EP4 receptor in Advillin lineage cells, referred to as  $EP4_{Avil}^{-/-}$  in the text). Heterozygous male *LysM-Cre* mice were crossed with an *iDTR<sup>fl/fl</sup>* mouse or a *COX2<sup>fl/fl</sup>* mouse. The offspring were intercrossed to generate the following genotypes: WT, *LysM-Cre*, *iDTR<sup>fl/fl</sup>*, *COX2<sup>fl/fl</sup>* mice (mice homozygous for COX2 flox allele, referred to as  $COX2^{wt}$  in the text), *LysM-Cre::iDTR<sup>fl/fl</sup>* (referred to as  $iDTR_{LysM}^{+/-}$  in the text), *LysM-Cre::COX2<sup>fl/fl</sup>* (conditional deletion of COX2 in monocyte-macrophage lineage, referred to as  $COX2_{LysM}^{-/-}$  in the text).

The genotypes of the mice were determined by polymerase chain reaction (PCR) analyses of the genomic DNA, which was extracted from mouse tails. The primers used for genotyping were Avil-Cre: Forward: CCCTGTTCACTGTGAGTAGG, Reverse: GCGATCCCTG AACATGTCCATC; LysM-Cre: Forward: CCCAGAAATGCCAGATTACG, Reverse: CTTGGGCTG CCAGAATTTCTC; TrkA loxP allele: Forward: AACAGTTTTGAGCATTCTATTGTTT, Reverse: CAAAGAAAACAGAAGAAAAAT AATAC; iDTR loxP allele: Forward: GCGAAGAGTTTGTCTCAACC, Reverse: AAAGTCGCTCT GAGTTGTTAT; COX2 loxP allele: Forward: AATTACTGCTGAAGCCCACC, Reverse: GAATCTC CTAGAACTGACTGG; EP4 loxP allele: Forward: TCTGTGAAGCGAGTCCTTAGGCT, Reverse: CG CACTCTCTCTCCCAAGGAA. All animals were maintained at the animal facility of The Johns Hopkins University School of Medicine. All animal experimental protocols and relevant ethical regulations were followed, and the study was approved by the Animal Care and Use Committee of The Johns Hopkins University, Baltimore, MD, USA.

### ***In vivo* treatment**

Twenty percent alginate gel (Alg) was prepared by mixing sodium alginate powder (Sigma-Aldrich, St. Louis, MO, USA) in deionized water, while 10% magnesium chloride (MgCl<sub>2</sub>, Sigma-Aldrich), 10% zinc chloride (ZnCl<sub>2</sub>, Sigma-Aldrich), and 10% copper chloride (CuCl<sub>2</sub>, Sigma-Aldrich) were used for the preparation of magnesium cross-linked alginate (Mg-Alg), zinc cross-linked alginate (Zn-Alg), and copper cross-linked alginate (Cu-Alg). Twelve-week-old male mice were anesthetized by intraperitoneal injection with ketamine (75 mg/kg) and xylazine (10 mg/kg). A longitudinal incision was made at the left knee and the patella was dislocated to expose the femoral condyle. Using a 20-gauge needle, we created a tunnel with a diameter of 1 mm from the patellofemoral groove of the distal femur along the axis of the femoral shaft. After thorough irrigation with saline, either pure alginate or divalent cation-releasing alginate was injected into the femoral canal. The wound was sutured, and the mice were housed in a specific-pathogen-free facility after the surgery. A monocyte-macrophage lineage depletion mouse model was induced by intraperitoneal injection of diphtheria toxin (DTX, Sigma-Aldrich) in iDTR<sub>LysM</sub><sup>+/-</sup> mice every other day during the week before and the week after the surgery. A PGE<sub>2</sub> degradation enzyme inhibitor, SW033291 (Selleck Chemicals, Houston, TX, USA), was administered by intraperitoneal injection at 10 mg/kg every day for 1 week after the surgery. A low-dose β-adrenergic receptor blocker, propranolol (PROP, Sigma-Aldrich, 1576005), was administered by intraperitoneal injection at 0.5 mg/kg every day for 1 week after the surgery.

### **μCT analysis**

At designated time points, the femurs were harvested from the mice and fixed overnight using 4% paraformaldehyde. Analysis was performed using a high-resolution μCT scanner (SkyScan 1275, Bruker, Kontich, Belgium). The voltage of the scanning procedure was 65 kv with a 153-μA current. The resolution

was set to 8.7  $\mu\text{m}$  per pixel. Two phantom-contained rods with a standard density of 0.25 and 0.75  $\text{g}/\text{cm}^3$  were scanned with each sample for calibration. Data reconstruction was completed using NRecon software (v1.6, SkyScan), data analysis was accomplished using CTAn software (v1.9, SkyScan), and 3D model visualization was performed using CTvox software (v3.2, SkyScan). Bone volume fraction (BV/TV), bone mineral density (BMD of TV), trabecular number (Tb. N), trabecular thickness (Tb. Th), cortical thickness (Ct. Th), cortical area (Ct. Ar), bone perimeter (B. Pm), and  $\rho$ -moment of inertia ( $\rho\text{MOI}$ ) were measured via  $\mu\text{CT}$  data.

## **Immunofluorescence and histomorphometric analysis**

At designated time points, mice femurs were fixed with 4% paraformaldehyde overnight and decalcified with 10% ethylenediaminetetraacetic acid (pH = 7.4) for 21 days. For immunostaining, the samples were dehydrated in 20% sucrose solution with 2% polyvinylpyrrolidone (PVP, Sigma-Aldrich) for 24 hours and embedded in 8% gelatin (Sigma-Aldrich) supplemented with 20% sucrose and 2% PVP. Forty- $\mu\text{m}$ -thick coronal-oriented sections of the femurs were obtained using a cryostat microtome. For histomorphometry, the samples were dehydrated in ethanol, embedded in paraffin, and prepared into 5- $\mu\text{m}$ -thick coronal-oriented sections using a rotary microtome. The brain and dorsal root ganglia (DRG) tissues harvested from the mice were fixed with 4% paraformaldehyde, dehydrated with 30% sucrose, and embedded in an optimal cutting temperature compound (OCT, Sakura Finetek, Torrance, CA, USA). Ten- $\mu\text{m}$ -thick coronal-oriented sections of the brain and DRG were obtained using a cryostat microtome.

Immunostaining was performed using a standard protocol. Briefly, the sections of the brain and DRG were incubated with primary antibodies to mouse OCN (Abcam, Cambridge, UK, ab93876, 1:200), CD68 (Abcam, ab31630, 1:400), CGRP (Abcam, ab81887, 1:300), PGP9.5 (Abcam, ab108986, 1:300), COX2 (Abcam, ab15191, 1:200), CREB (Abcam, 178322, 1:200), p-CREB (Abcam, ab32096, 1:200), and TH (MilliporeSigma, Burlington, MA, USA, AB152, 1:100) overnight at 4°C. Alexa-Fluor 488-conjugated and Alexa-Fluor 647-conjugated secondary antibodies (Thermo Fisher Scientific, Waltham, MA, USA) were used for immunofluorescent staining, while the nuclei were counterstained with Hoechst 33324 (Thermo Fisher Scientific). Immunofluorescent images were captured using a LSM 780 confocal microscope (Zeiss, Oberkochen, Germany). Hematoxylin and eosin (H&E) staining, Safranin O and fast green staining, and TRAP staining (Sigma-Aldrich) were performed in selected slides from each sample according to the manufacturer's instructions. Images were captured using a polarized light microscope (Nikon Eclipse VL100POL, Tokyo, Japan), and quantitative histomorphometric analysis was performed using Image J software (v.1.5, National Institutes of Health, Bethesda, MD, USA).

## **Cell culture**

Primary BMM and DRG neurons from 4-week-old mice were isolated. After the mice were euthanized, both femurs were dissected to remove soft tissue. The femurs were then crushed into pieces and digested with  $\alpha$ -MEM (Minimum Essential Medium Eagle  $\alpha$  Modification) containing 3 mg/mL collagenase I (Worthington Biochemical Corp, Lakewood, NJ, USA), 4 mg/mL dispase (Sigma-Aldrich), and 1 U/mL deoxyribonuclease-I (Invitrogen, Thermo Fisher Scientific). The single-cell suspension was achieved by passing the solution through a cell strainer to remove tissue fragments. After incubation in a humidified incubator with 5% CO<sub>2</sub> at 37°C, the non-adherent cells were harvested and cultured in  $\alpha$ -MEM supplemented with 20 ng/mL macrophage colony-stimulating factor (M-CSF, R&D Systems, Minneapolis, MN, USA) for 7 days. For the primary culture of DRG neurons, DRGs from the L2–L5 spinal levels were isolated in cold DMEM/F12 (Dulbecco's Modified Eagle Medium/Nutrient Mixture F-12) medium (Invitrogen, Thermo Fisher Scientific) and then digested with 1mg/mL collagenase type A (Roche, Basel, Switzerland) at 37°C. After trituration and centrifugation, cells were resuspended and seeded on glass coverslips coated with poly-D-lysine and laminin. The culture medium was replaced 6 hours after seeding, and the adherent cells were further cultured at 37°C with 5% CO<sub>2</sub> for 3 days before use.

## **ELISA**

Whole blood samples were collected by cardiac puncture immediately after the mice were euthanized. Serum was collected by centrifuging at 200 rpm for 15 minutes and then stored at -80°C before analysis. The total bone protein was harvested from the femurs grafted with pure alginate or Mg-Alg. The mid-shaft of the femur, approximately 1 cm long, was ground into mud using a ceramic mortar and pestle under cooling. The mud of the bone tissue was then homogenized in pre-cooled radioimmunoprecipitation assay (RIPA) lysis and extraction buffer (Thermo Fisher Scientific) for 1 hour. The buffer solution was centrifuged at 15,000 rpm for 20 minutes at 4°C. The supernatant was collected for protein concentration quantification with the BCA Protein Assay Kit (Thermo Fisher Scientific). An equal amount of protein from each sample was subjected to quantitative analysis using a specific ELISA kit per the manufacturer's instruction. The PGE<sub>2</sub> concentrations in the serum and bone marrow were determined by the PGE<sub>2</sub> ELISA kit (Cayman Chemical, Ann Arbor, MI, USA). The OCN level was determined by an OCN ELISA kit (Biomedical Technologies Inc, Tewksbury, MA, USA). The serum and urine epinephrine levels were determined by an epinephrine ELISA kit (ALPCO, Salem, NH, USA).

## **Quantitative real-time polymerase chain reaction (qPCR)**

The total RNA of the cells was extracted and purified using the RNeasy Plus kit (Qiagen, Germantown, MD, USA) per the manufacturer's instructions. For the reverse transcription, complementary DNA was synthesized using the SuperScript First-Strand Synthesis System (Invitrogen, Thermo Fisher Scientific). The primers used in the RT–qPCR assay were synthesized by Life Technologies (Thermo Fisher Scientific) based on sequences retrieved from Primer Bank (<http://pga.mgh.harvard.edu/primerbank>,

Supplementary Table 1). SYBR Green-Master Mix (Qiagen, Germantown, MD, USA) was used for the amplification and detection of complementary DNA on a C1000 Thermal Cycler (Bio-Rad Laboratories, Hercules, CA). The mean cycle threshold (Ct) value of each target gene was normalized to the housekeeping gene glyceraldehyde-3-phosphate dehydrogenase (*GAPDH*). The results were shown as a fold change using the  $\Delta\Delta C_t$  method.

## Western blot

The total protein from animal tissues or cell cultures was lysed using RIPA lysis and extraction buffer (Thermo Fisher Scientific) supplemented with a protease inhibitor cocktail (Thermo Fisher Scientific). After centrifugation at  $15,000 \times g$  for 10 minutes at  $4^\circ\text{C}$ , the supernatants were collected to measure the protein concentration with the BCA Protein Assay Kit (Thermo Fisher Scientific). A total of  $30 \mu\text{g}$  of protein was subjected to sodium dodecyl sulfate–polyacrylamide gel electrophoresis and then blotted on the nitrocellulose membranes (Bio-Rad Laboratories). The membrane was blocked in 5% w/v bovine serum albumin (BSA, Sigma-Aldrich) and incubated with blocking buffer-diluted primary antibodies overnight at  $4^\circ\text{C}$ . The primary antibodies used were CREB (Abcam, 178322), p-CREB (Abcam, ab32096), HTR2C (ab197776), COX2 (Abcam, ab15191), p-I $\kappa$ B $\alpha$  (CST, 2859), I $\kappa$ B $\alpha$  (CST, 4814), p-NF- $\kappa$ B p65 (CST, 3033), NF- $\kappa$ B p65 (CST, 8242), and  $\beta$ -actin (CST, 3700). The proteins were visualized by an enhanced chemiluminescence kit (Amersham Bioscience, Little Chalfont, UK) and exposed under a ChemiDoc XRS System (Bio-Rad Laboratories).

## Behavioral analysis

The spontaneous activity of mice after surgery was assessed using spontaneous activity wheels (BIO-ACTIVW-M, Bioseb, Boulogne, France). Mice were housed in polycarbonate cages with free access to stainless steel activity wheels (diameter 23 cm; width 5 cm), which were connected to an analyzer that automatically recorded the distance traveled, mean speed, maximum speed, and total active time. The mice had *ad libitum* access to food and water during the test. They were allowed to acclimatize to the environment for at least 24 hours before data were recorded.

## Chromatin immunoprecipitation (ChIP) assay

After the stimulation, the ChIP assay was performed using an Agarose ChIP Kit (Thermo Fisher Scientific) according to the manufacturer's instructions. In brief, the chromatin was cross-linked by 1% formaldehyde and digested by micrococcal nuclease. The lysate was incubated with rabbit anti-NF- $\kappa$ B p65 at  $4^\circ\text{C}$  overnight followed by incubation with ChIP Grade Protein A/G Plus Agarose. The purified DNA was analyzed by PCR assay using primers targeting mouse COX2 promoters: sense 5'-

CCCGGAGGGTAGTTCCATGAAAGACTTCAAC-3' and antisense 5'-GGTGGAGCTGGCAGGATGCAGTCCTG-3'. The primers targeting the *GAPDH* promoter served as a positive control. PCR products obtained after 40 cycles were separated on 2% agarose gels.

## Statistical analysis

All data analyses were performed and illustrated using Prism software (v. 7, GraphPad Software, San Diego, CA, USA). Data are presented as means  $\pm$  standard deviations (SD). For comparisons between 2 groups, 2-tailed Student's T-tests were used. For comparisons among multiple groups, 1-way or 2-way analysis of variance (ANOVA) was used, followed by Tukey's post hoc test. Significant differences among groups were defined and noted as  $*P < 0.05$  or  $**P < 0.01$ . Sample size was based on preliminary data, as well as on observed effect sizes.

## Declarations

### Acknowledgments

We acknowledge the HKU Li Ka Shing Faculty of Medicine Faculty Core Facility for providing a harmonious working environment. For their editorial assistance, we thank Jenni Weems, MS, Kerry Kennedy, BA, and Rachel Box, MS, in the Editorial Services group of The Johns Hopkins Department of Orthopaedic Surgery. This work is jointly supported by the National Key R&D Program of China (R&D#2018YFA0703100), Hong Kong Research Grant Council (grants 17207719, 17214516 and N\_HKU725/16), Hong Kong Health and Medical Research Fund (19180712), Shenzhen Science and Technology Funding (JSGG20180507183242702), HKU-SZH Fund for Shenzhen Key Medical Discipline (SZXK2020084) and Sanming Project of Medicine in Shenzhen "Team of Excellence in Spinal Deformities and Spinal Degeneration" (SZSM201612055).

### Author contributions

W. Qiao performed animal surgery, cell culture, and the *in vitro* and *in vivo* tests. D. Pan contributed to the data analysis. Y. Zheng, S. Wu, and X. Liu provide insightful comments on the material-science related issues. K.M.C. Cheung and Z.F. Chen contributed to the design of animal models and provided invaluable suggestions about clinical indications of the study. J.P. Matinlinna, M. Wan, and S. Feng contributed to the experiment design and data interpretation. X. Cao and K.W.K. Yeung contributed to data interpretation and supervised the project. W. Qiao, X. Cao, and K.W.K. Yeung wrote the manuscript with input from all authors.

## Competing interests

The authors declare no competing interests.

## Data and materials availability

All data associated with this study are present in the paper or the Supplementary Information.

## References

1. Liu, Y., *et al.* Biodegradable metal-derived magnesium and sodium enhances bone regeneration by angiogenesis aided osteogenesis and regulated biological apatite formation. *Chem Eng J* **410**(2021).
2. Lin, S.H., *et al.* A Magnesium-Enriched 3D Culture System that Mimics the Bone Development Microenvironment for Vascularized Bone Regeneration. *Adv Sci* **6**(2019).
3. Han, H.S., *et al.* Biodegradable Magnesium Alloys Promote Angio-Osteogenesis to Enhance Bone Repair. *Adv Sci* **7**(2020).
4. Qiao, W., *et al.* TRPM7 kinase-mediated immunomodulation in macrophage plays a central role in magnesium ion-induced bone regeneration. *Nat Commun* **12**, 2885 (2021).
5. Liu, W., *et al.* Zinc-Modified Sulfonated Polyetheretherketone Surface with Immunomodulatory Function for Guiding Cell Fate and Bone Regeneration. *Adv Sci* **5**, 1800749 (2018).
6. Bari, A., *et al.* Copper-containing mesoporous bioactive glass nanoparticles as multifunctional agent for bone regeneration. *Acta Biomater* **55**, 493–504 (2017).
7. Yang, F., *et al.* A GABAergic neural circuit in the ventromedial hypothalamus mediates chronic stress-induced bone loss. *J Clin Invest* **130**, 6539–6554 (2020).
8. Eleftheriou, F., *et al.* Leptin regulation of bone resorption by the sympathetic nervous system and CART. *Nature* **434**, 514–520 (2005).
9. Yadav, V.K., *et al.* A serotonin-dependent mechanism explains the leptin regulation of bone mass, appetite, and energy expenditure. *Cell* **138**, 976–989 (2009).
10. Chen, H., *et al.* Prostaglandin E2 mediates sensory nerve regulation of bone homeostasis. *Nat Commun* **10**, 181 (2019).
11. Chen, W.G., *et al.* The Emerging Science of Interoception: Sensing, Integrating, Interpreting, and Regulating Signals within the Self. *Trends Neurosci* **44**, 3–16 (2021).
12. Salvador, A.F., de Lima, K.A. & Kipnis, J. Neuromodulation by the immune system: a focus on cytokines. *Nat Rev Immunol* (2021).
13. Rinaman, L. Visceral sensory inputs to the endocrine hypothalamus. *Front Neuroendocrinol* **28**, 50–60 (2007).

14. Marrella, A., *et al.* Engineering vascularized and innervated bone biomaterials for improved skeletal tissue regeneration. *Materials Today* **21**, 362–376 (2018).
15. Thakur, M., Dickenson, A.H. & Baron, R. Osteoarthritis pain: nociceptive or neuropathic? *Nat Rev Rheumatol* **10**, 374–380 (2014).
16. Haralrie, F., Amizuka, N. & Ozawa, H. Immunohistochemical and ultrastructural localization of CGRP-Positive nerve fibers at the epiphyseal trabecules facing the growth plate of rat femurs. *Bone* **18**, 29–39 (1996).
17. Mach, D.B., *et al.* Origins of skeletal pain: sensory and sympathetic innervation of the mouse femur. *Neuroscience* **113**, 155–166 (2002).
18. Ortuno, M.J., *et al.* Serotonin-reuptake inhibitors act centrally to cause bone loss in mice by counteracting a local anti-resorptive effect. *Nat Med* **22**, 1170–1179 (2016).
19. Hu, B., *et al.* Sensory nerves regulate mesenchymal stromal cell lineage commitment by tuning sympathetic tones. *J Clin Invest* **130**, 3483–3498 (2020).
20. Xiao Lv, F.G., Tuo Peter Li, Peng Xue, Xiao Wang, Mei Wan, Bo Hu, Hao Chen, Zengwu Shao, Xu Cao. Skeleton Interoception Regulates Bone and Fat Metabolism through Hypothalamic Neuroendocrine NPY. *Elife* (2021).
21. Peng Xue, S.W., Xiao Lyu, Mei Wan, Xialin Li, Lei Ma, Neil C. Ford,, Yuku Li, Yun Guan, Wenyuan Ding, Xu Cao. Skeleton Interoception Activity Reduces Vertebral Endplate Porosity and Spinal Pain with Low-Dose Celecoxib. *Bone Research* (2021).
22. Ni, S., *et al.* Sensory innervation in porous endplates by Netrin-1 from osteoclasts mediates PGE2-induced spinal hypersensitivity in mice. *Nat Commun* **10**, 5643 (2019).
23. Einhorn, T.A. & Gerstenfeld, L.C. Fracture healing: mechanisms and interventions. *Nat Rev Rheumatol* **11**, 45–54 (2015).
24. Loi, F., *et al.* Inflammation, fracture and bone repair. *Bone* **86**, 119–130 (2016).
25. Claes, L., Recknagel, S. & Ignatius, A. Fracture healing under healthy and inflammatory conditions. *Nat Rev Rheumatol* **8**, 133–143 (2012).
26. Uppal, S., *et al.* Mutations in 15-hydroxyprostaglandin dehydrogenase cause primary hypertrophic osteoarthropathy. *Nat Genet* **40**, 789–793 (2008).
27. Zhang, Y., *et al.* TISSUE REGENERATION. Inhibition of the prostaglandin-degrading enzyme 15-PGDH potentiates tissue regeneration. *Science* **348**, aaa2340 (2015).
28. Coggins, K.G., *et al.* Metabolism of PGE2 by prostaglandin dehydrogenase is essential for remodeling the ductus arteriosus. *Nat Med* **8**, 91–92 (2002).
29. Yuksel-Konuk, B., *et al.* Homozygous mutations in the 15-hydroxyprostaglandin dehydrogenase gene in patients with primary hypertrophic osteoarthropathy. *Rheumatol Int* **30**, 39–43 (2009).
30. Kuner, R. Central mechanisms of pathological pain. *Nat Med* **16**, 1258–1266 (2010).
31. Zhu, S., *et al.* Subchondral bone osteoclasts induce sensory innervation and osteoarthritis pain. *J Clin Invest* **129**, 1076–1093 (2019).

32. Seidenberg, A.B. & An, Y.H.H. Is there an inhibitory effect of COX-2 inhibitors on bone healing? *Pharmacological Research* **50**, 151–156 (2004).
33. Radi, Z.A. & Khan, N.K. Effects of cyclooxygenase inhibition on bone, tendon, and ligament healing. *Inflamm Res* **54**, 358–366 (2005).
34. Franz, S., Rammelt, S., Scharnweber, D. & Simon, J.C. Immune responses to implants - a review of the implications for the design of immunomodulatory biomaterials. *Biomaterials* **32**, 6692–6709 (2011).
35. Chen, Z., *et al.* Osteoimmunomodulation for the development of advanced bone biomaterials. *Materials Today* **19**, 304–321 (2015).
36. Zhang, J., *et al.* Magnesium modification of a calcium phosphate cement alters bone marrow stromal cell behavior via an integrin-mediated mechanism. *Biomaterials* **53**, 251–264 (2015).
37. Wong, H.M., *et al.* Low-modulus Mg/PCL hybrid bone substitute for osteoporotic fracture fixation. *Biomaterials* **34**, 7016–7032 (2013).
38. Lin, Z., *et al.* Precisely controlled delivery of magnesium ions thru sponge-like monodisperse PLGA/nano-MgO-alginate core-shell microsphere device to enable in-situ bone regeneration. *Biomaterials* **174**, 1–16 (2018).
39. Ren, L., Wong, H.M., Yan, C.H., Yeung, K.W. & Yang, K. Osteogenic ability of Cu-bearing stainless steel. *Journal of Biomedical Materials Research Part B: Applied Biomaterials* **103**, 1433–1444 (2015).
40. Chaigne-Delalande, B. & Lenardo, M.J. Divalent cation signaling in immune cells. *Trends Immunol* **35**, 332–344 (2014).
41. Li, Z., *et al.* Fracture repair requires TrkA signaling by skeletal sensory nerves. *J Clin Invest* **129**, 5137–5150 (2019).
42. Oury, F., *et al.* CREB mediates brain serotonin regulation of bone mass through its expression in ventromedial hypothalamic neurons. *Genes & Development* **24**, 2330–2342 (2010).
43. Yoshida, K., *et al.* Stimulation of bone formation and prevention of bone loss by prostaglandin E EP4 receptor activation. *Proc Natl Acad Sci U S A* **99**, 4580–4585 (2002).
44. Zhang, Y., *et al.* Implant-derived magnesium induces local neuronal production of CGRP to improve bone-fracture healing in rats. *Nature medicine* **22**, 1160 (2016).
45. Yang, H.T., *et al.* Alloying design of biodegradable zinc as promising bone implants for load-bearing applications. *Nature Communications* **11**(2020).
46. Shi, M., *et al.* Copper-doped mesoporous silica nanospheres, a promising immunomodulatory agent for inducing osteogenesis. *Acta Biomater* **30**, 334–344 (2016).
47. Jee, W.S., Mori, S., Li, X.J. & Chan, S. Prostaglandin E2 enhances cortical bone mass and activates intracortical bone remodeling in intact and ovariectomized female rats. *Bone* **11**, 253–266 (1990).
48. Xie, C., *et al.* COX-2 from the injury milieu is critical for the initiation of periosteal progenitor cell mediated bone healing. *Bone* **43**, 1075–1083 (2008).
49. Stafford, S.L., *et al.* Metal ions in macrophage antimicrobial pathways: emerging roles for zinc and copper. *Biosci Rep* **33**(2013).

50. Lima, F.D., *et al.* An insight into the role of magnesium in the immunomodulatory properties of mesenchymal stem cells. *Journal of Nutritional Biochemistry* **55**, 200–208 (2018).
51. Arancibia, S., Barrientos, A., Torrejon, J., Escobar, A. & Beltran, C.J. Copper oxide nanoparticles recruit macrophages and modulate nitric oxide, proinflammatory cytokines and PGE(2) production through arginase activation. *Nanomedicine* **11**, 1237–1251 (2016).
52. Roy, R., *et al.* ZnO nanoparticles induced adjuvant effect via toll-like receptors and Src signaling in Balb/c mice. *Toxicol Lett* **230**, 421–433 (2014).
53. Zhou, Q., *et al.* Influence of different divalent ions cross-linking sodium alginate-polyacrylamide hydrogels on antibacterial properties and wound healing. *Carbohydrate Polymers* **197**, 292–304 (2018).
54. Wong, H.M., *et al.* In vivo stimulation of bone formation by aluminum and oxygen plasma surface-modified magnesium implants. *Biomaterials* **34**, 9863–9876 (2013).
55. Li, B., *et al.* In vitro and in vivo responses of macrophages to magnesium-doped titanium. *Sci Rep* **7**, 42707 (2017).
56. Wang, M., *et al.* Improved osteogenesis and angiogenesis of magnesium-doped calcium phosphate cement via macrophage immunomodulation. *Biomater Sci* **4**, 1574–1583 (2016).
57. Baldwin Jr, A.S. The NF- $\kappa$ B and I $\kappa$ B proteins: new discoveries and insights. *Annual review of immunology* **14**, 649–681 (1996).
58. Orwoll, E.S. Toward an expanded understanding of the role of the periosteum in skeletal health. *J Bone Miner Res* **18**, 949–954 (2003).
59. Gao, B., *et al.* Macrophage-lineage TRAP + cells recruit periosteum-derived cells for periosteal osteogenesis and regeneration. *J Clin Invest* **129**, 2578–2594 (2019).
60. Dimitriou, R., Tsiridis, E. & Giannoudis, P.V. Current concepts of molecular aspects of bone healing. *Injury* **36**, 1392–1404 (2005).
61. Niedermair, T., *et al.* Absence of substance P and the sympathetic nervous system impact on bone structure and chondrocyte differentiation in an adult model of endochondral ossification. *Matrix Biology* **38**, 22–35 (2014).
62. Chartier, S.R., *et al.* Exuberant sprouting of sensory and sympathetic nerve fibers in nonhealed bone fractures and the generation and maintenance of chronic skeletal pain. *Pain* **155**, 2323–2336 (2014).
63. Basbaum, A.I., Bautista, D.M., Scherrer, G. & Julius, D. Cellular and molecular mechanisms of pain. *Cell* **139**, 267–284 (2009).
64. Tomlinson, R.E., *et al.* NGF-TrkA signaling in sensory nerves is required for skeletal adaptation to mechanical loads in mice. *Proceedings of the National Academy of Sciences of the United States of America* **114**, E3632-E3641 (2017).
65. Schweitzer, M.H., Wittmeyer, J.L., Horner, J.R. & Toporski, J.K. Soft-tissue vessels and cellular preservation in *Tyrannosaurus rex*. *Science* **307**, 1952–1955 (2005).

66. Smit, T.H., Huyghe, J.M. & Cowin, S.C. Estimation of the poroelastic parameters of cortical bone. *J Biomech* **35**, 829–835 (2002).
67. Takeda, S., *et al.* Leptin regulates bone formation via the sympathetic nervous system. *Cell* **111**, 305–317 (2002).
68. Elefteriou, F. Impact of the Autonomic Nervous System on the Skeleton. *Physiol Rev* **98**, 1083–1112 (2018).

## Figures

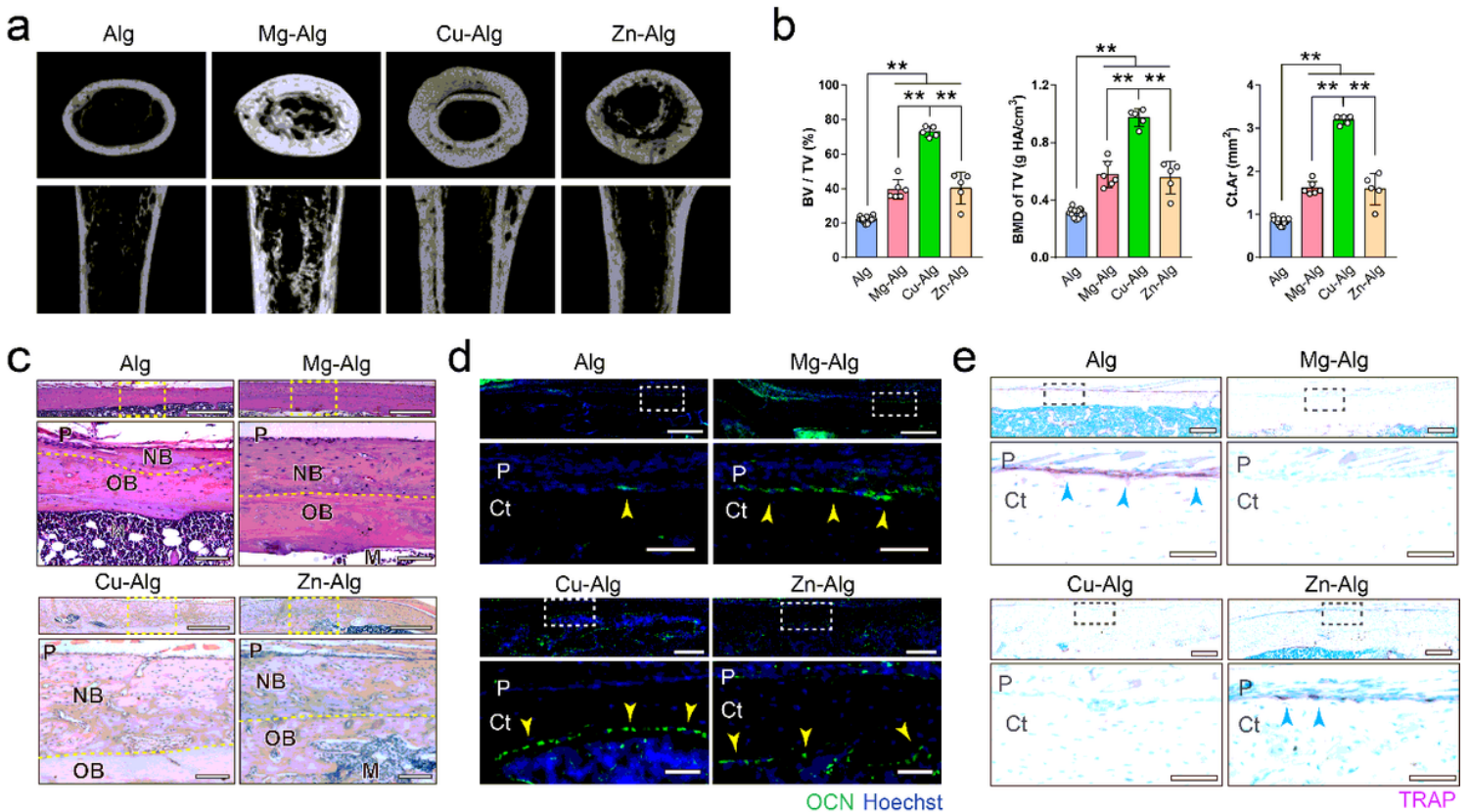


**Figure 1**

Divalent cations released from alginate induce new bone formation. (a) Reconstructed micro-computed tomography ( $\mu$ CT) images showing the new bone formation in mouse femurs grafted with  $Mg^{2+}$ -,  $Cu^{2+}$ -, or  $Zn^{2+}$ -releasing alginate. Pure alginate grafted mice serve as control. (b) Corresponding measurements of bone volume fraction (BV/TV), bone mineral density (BMD of TV), and cortical bone area (Ct.Ar). (c) Representative images of hematoxylin and eosin (H&E) staining showing periosteal new bone formation. Lower images (scale bars = 100  $\mu$ m) are high-resolution versions of the boxed regions in the upper images (scale bars = 500  $\mu$ m). P, periosteum; NB, new bone; OB, old bone; M, marrow. (d) Representative immunofluorescent images showing the presence of osteocalcin+ (OCN+) osteoblasts on the cortical bone surface. Lower images (scale bars = 50  $\mu$ m) are high-resolution versions of the boxed regions in the upper images (scale bars = 200  $\mu$ m). P, periosteum; Ct, cortical bone. (e) Representative images of

tartrate-resistant acid phosphatase (TRAP) staining showing the presence of TRAP+ osteoclasts on the cortical bone surface. Lower images (scale bars = 100  $\mu\text{m}$ ) are high-resolution versions of the boxed regions in the upper images (scale bars = 400  $\mu\text{m}$ ). Data are mean  $\pm$  standard deviation (s.d.)  $**P < 0.01$  by 1-way analysis of variance (ANOVA) with Tukey's post hoc test.

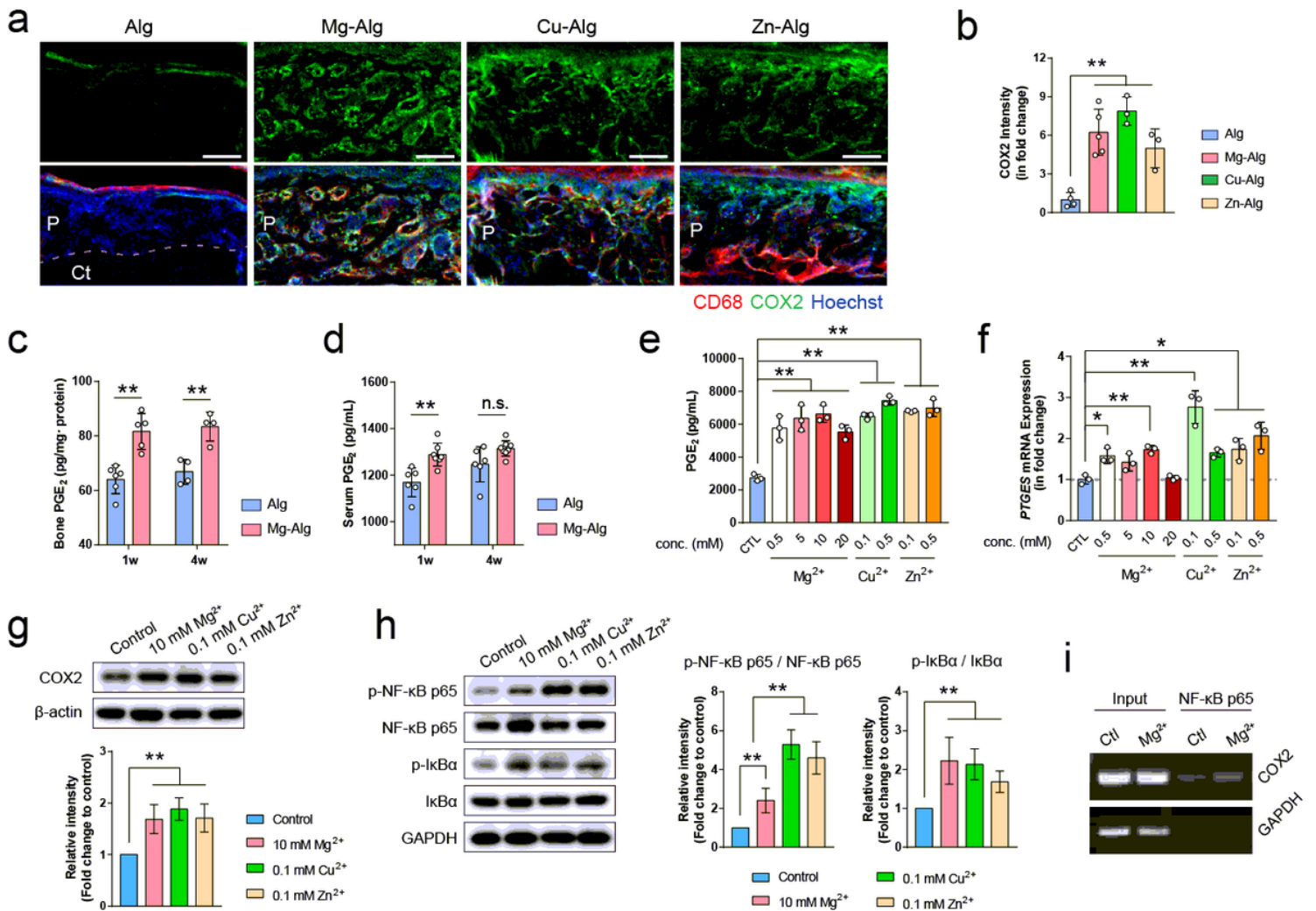


**Figure 2**

Divalent cations stimulate secretion of prostaglandin E2 (PGE<sub>2</sub>) by macrophages. (a) Co-immunostaining of cyclooxygenase-2 (COX2) with cluster of differentiation 68 (CD68) in the periosteum at week 1 postoperatively (scale bars = 100  $\mu\text{m}$ ). (b) Quantification of COX2 intensity in the periosteum at week 1 postoperatively. (c, d) Enzyme-linked immunosorbent assay (ELISA) analysis of the bone (c) and serum (d) PGE<sub>2</sub> concentration at week 1 and week 4 postoperatively. (e) ELISA analysis showing the effect of different concentrations of Mg<sup>2+</sup>, Zn<sup>2+</sup>, or Cu<sup>2+</sup> on the release of PGE<sub>2</sub> from bone marrow macrophages (BMM). (f) Real-time polymerase chain reaction analysis of PTGES mRNA expression in mouse BMM after 3-day incubation culture medium supplemented with different concentrations of Mg<sup>2+</sup>, Zn<sup>2+</sup>, or Cu<sup>2+</sup>. (g) Representative Western blots and corresponding quantification showing the effect of different divalent cations on the expression of COX2 in mouse BMM. (h) Representative Western blots and corresponding quantification showing the effect of different divalent cations on the phosphorylation of

NF- $\kappa$ B and I $\kappa$ B $\alpha$  in mouse BMM. (i) Chromatin immunoprecipitation assay showing that the NF- $\kappa$ B p65 at the COX2 promoter was upregulated by the stimulation of Mg<sup>2+</sup>. Data are mean  $\pm$  s.d. n.s. (nonsignificant), \*P<0.05, \*\*P<0.01 by 1-way ANOVA with Tukey's post hoc test (b, e, f, g, h) or 2-way ANOVA with Tukey's post hoc test (c, d).

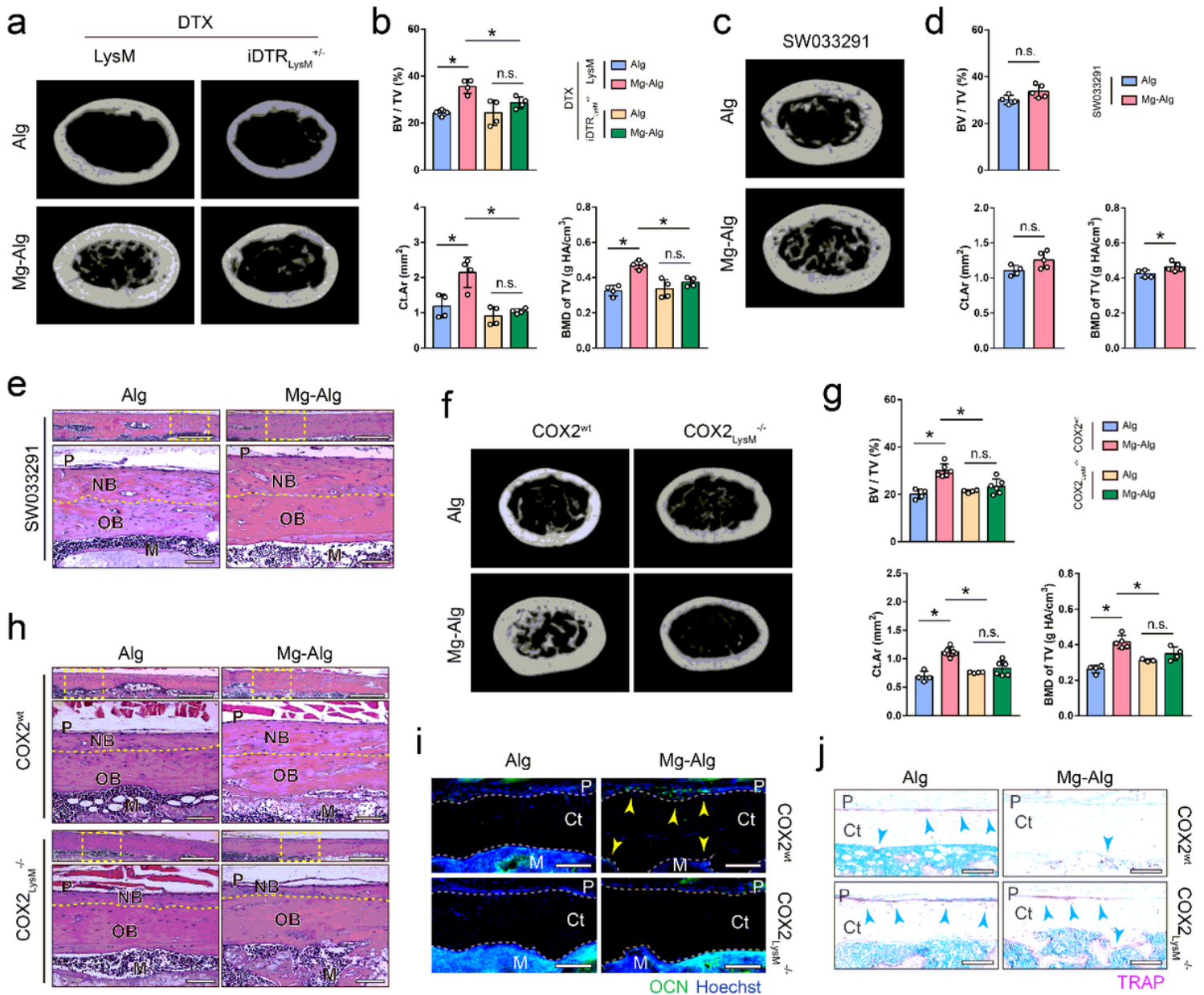


**Figure 3**

Macrophage-derived PGE<sub>2</sub> mediates divalent cation-induced bone formation. (a, b) Reconstructed  $\mu$ CT images (a) showing the cross-section of LysM or iDTRLysM<sup>+/-</sup> mouse femurs after the administration of diphtheria toxin and corresponding measurements (b) of BV/TV, BMD of TV, and Ct.Ar. (c, d) Reconstructed  $\mu$ CT images (c) showing the cross-section of mouse femurs after the administration of SW033291 and corresponding measurements (d) of BV/TV, BMD of TV, and Ct.Ar. (e) Representative H&E staining images showing periosteal new bone formation in SW033291-injected mice. Lower images (scale bars = 100  $\mu$ m) are high-resolution versions of the boxed regions in the upper images (scale bars =

500  $\mu\text{m}$ ). (f, g) Reconstructed  $\mu\text{CT}$  images (f) showing the cross-section of femurs from COX2wt mice or COX2LysM $^{-/-}$  mice grafted with pure alginate or Mg $^{2+}$ -releasing alginate, as well as corresponding measurements (g) of BV/TV, BMD of TV, and Ct.Ar. (h) Representative H&E staining images showing the periosteal new bone formation in COX2wt or COX2LysM $^{-/-}$  mice. Lower images (scale bars = 100  $\mu\text{m}$ ) are high-resolution versions of the boxed regions in the upper images (scale bars = 500  $\mu\text{m}$ ). (i) Representative immunofluorescent images showing the presence of OCN+ osteoblasts on the cortical bone surface (scale bars = 100  $\mu\text{m}$ ). (j) Representative TRAP staining images showing the presence of TRAP+ osteoclasts on the cortical bone surface (scale bars = 100  $\mu\text{m}$ ). Data are mean  $\pm$  s.d., \* $P$ <0.05, \*\* $P$ <0.01 by 1-way ANOVA with Tukey's post hoc test (b, g) or Student's T-test (d).

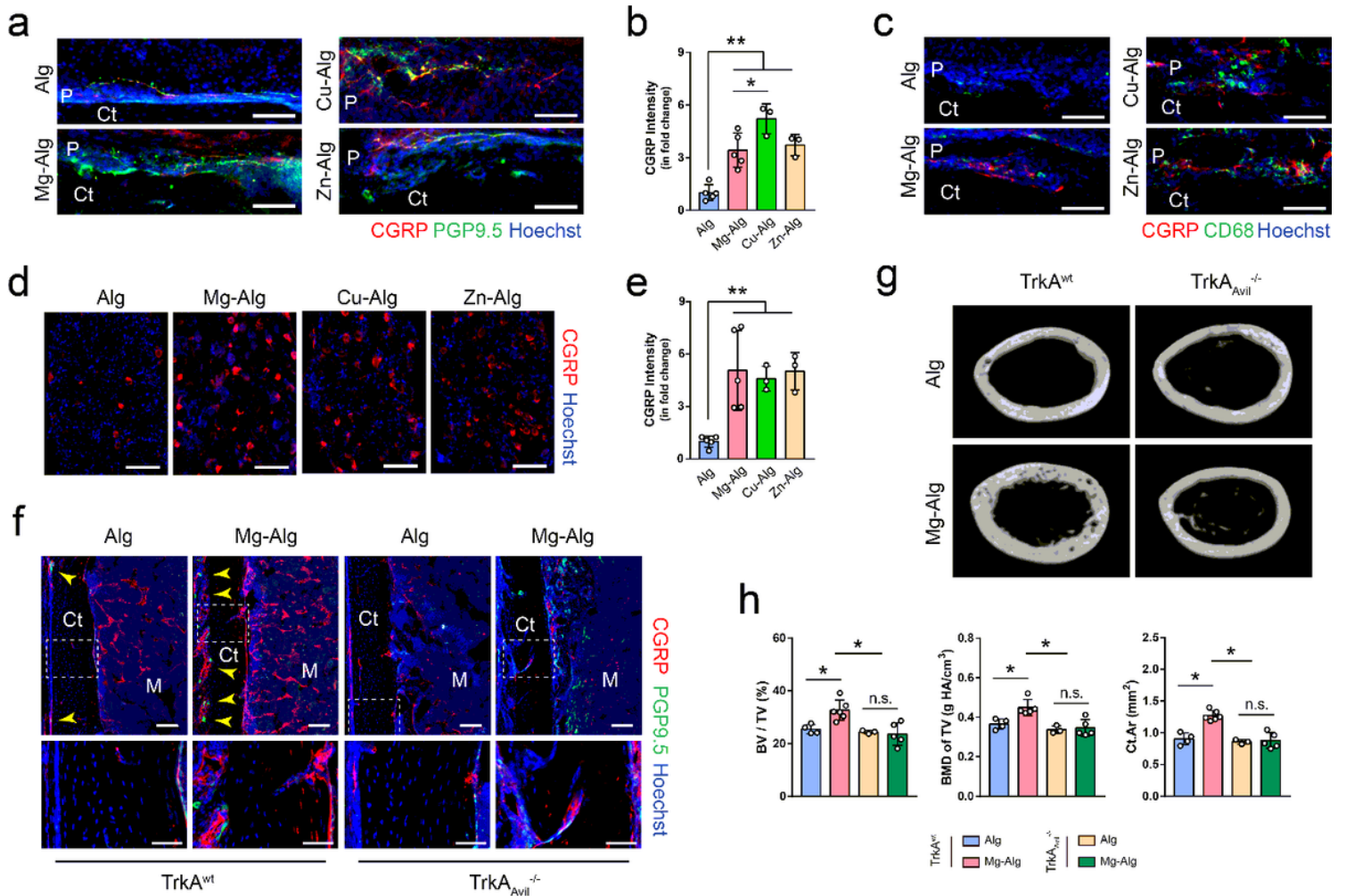


**Figure 4**

Deletion of sensory nerve abolishes divalent cation-induced bone formation. (a) Representative immunofluorescent images showing the sprouting and arborization of calcitonin gene-related polypeptide- $\alpha$  (CGRP+) sensory nerves within the periosteum at week 1 postoperatively (scale bars = 100  $\mu\text{m}$ ). (b) Quantification of CGRP intensity in the periosteum at week 1 postoperatively. (c) Co-immunostaining of CGRP with CD68 in the periosteum at week 1 postoperatively (scale bars = 100  $\mu\text{m}$ ). (d) Representative immunofluorescent images showing the expression of CGRP in DRGs of L4 lumbar at week 1 postoperatively (scale bars = 100  $\mu\text{m}$ ). (e) Quantification of CGRP intensity in DRGs at week 1

postoperatively. (f) Representative immunofluorescent images showing the presence of CGRP+ sensory nerves in the femurs of *TrkAwt* or *TrkAAvil-/-* mice. Lower images (scale bars = 50  $\mu$ m) are high-resolution versions of the boxed regions in the upper images (scale bars = 100  $\mu$ m). (g, h) Reconstructed  $\mu$ CT images (g) showing the cross-section of femurs from *TrkAwt* mice or *TrkAAvil-/-* mice grafted with pure alginate or Mg<sup>2+</sup>-releasing alginate and corresponding measurements (h) of BV/TV, BMD of TV, and Ct.Ar. Data are mean  $\pm$  s.d., \**P*<0.05, \*\**P*<0.01 by 1-way ANOVA with Tukey's post hoc test.

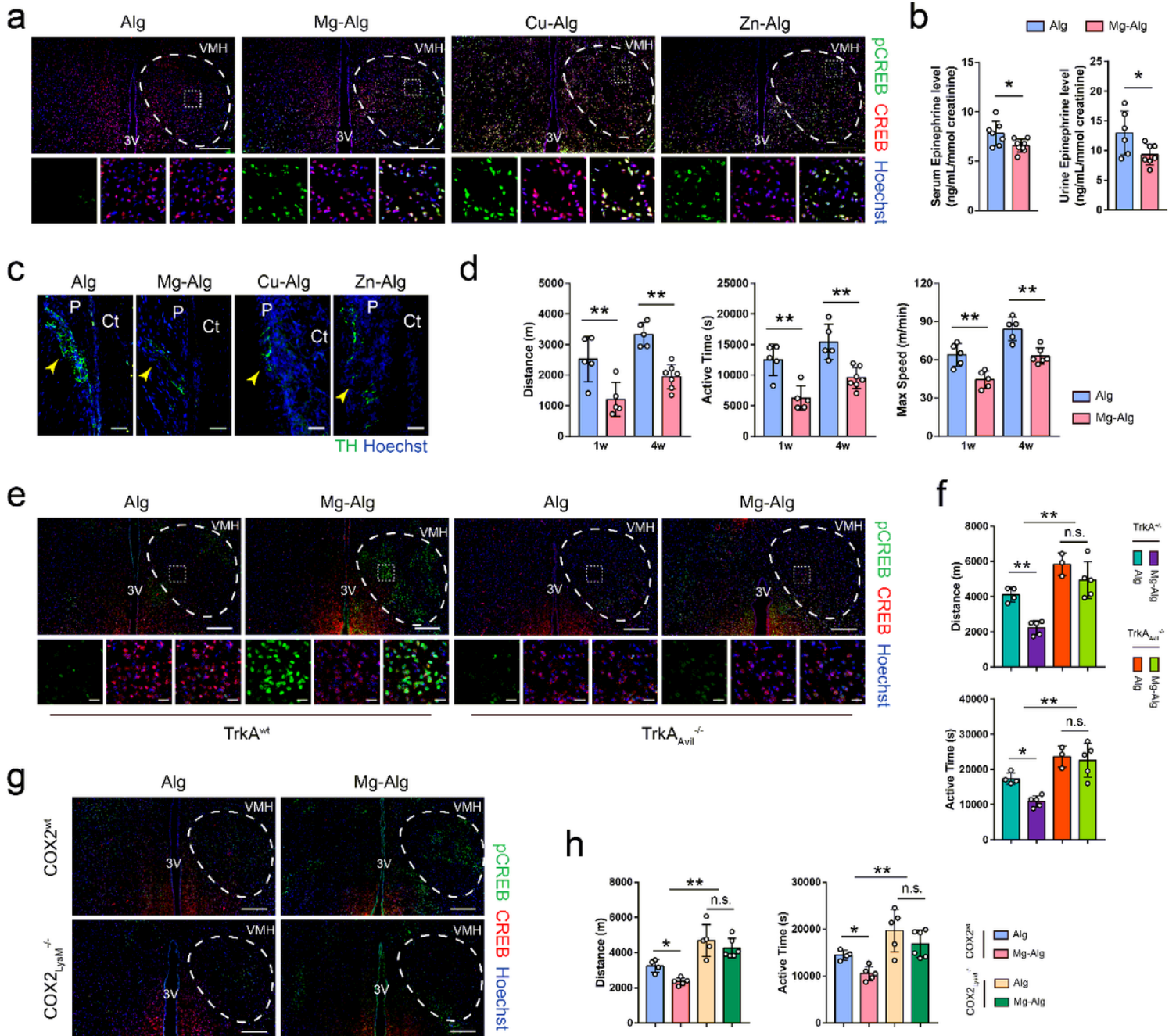


**Figure 5**

Divalent cations downregulate sympathetic activity through hypothalamic CREB signaling. (a) Representative immunofluorescent images showing the phosphorylation of CREB in the ventromedial hypothalamus (VMH) 1 week postoperatively. Lower images (scale bars = 20  $\mu$ m) are high-resolution

versions of the boxed regions in the upper images (scale bars = 200  $\mu\text{m}$ ). (b) ELISA of serum and urine epinephrine levels of mice at week 1 postoperatively. (c) Representative immunofluorescent images showing the presence of tyrosine-hydroxylase+ (TH+) sympathetic fibers on cortical bone surface (scale bars = 50  $\mu\text{m}$ ). (d) The daily distance (m), duration (s), and maximum speed of running-wheel activity of WT mice at weeks 1 and 4 postoperatively. (e, g) Representative immunofluorescent images showing the phosphorylation of CREB in the VMH of TrkAwt or TrkAAvil<sup>-/-</sup> mice (e), as well as COX2wt or COX2LysM<sup>-/-</sup> mice (g) at week 1 postoperatively. Lower images (scale bars = 20  $\mu\text{m}$ ) are high-resolution versions of VMH regions in the upper images (scale bars = 200  $\mu\text{m}$ ). (f, h) The daily distance (m) and duration (s) of running-wheel activity of TrkAwt mice or TrkAAvil<sup>-/-</sup> (f), as well as COX2wt or COX2LysM<sup>-/-</sup> (h) mice at week 4 postoperatively. Data are mean  $\pm$  s.d. \*P<0.05, \*\*P<0.01 by Student's T-test (b), 2-way ANOVA with Tukey's post hoc test (d), or 1-way ANOVA with Tukey's post hoc test (f, h).

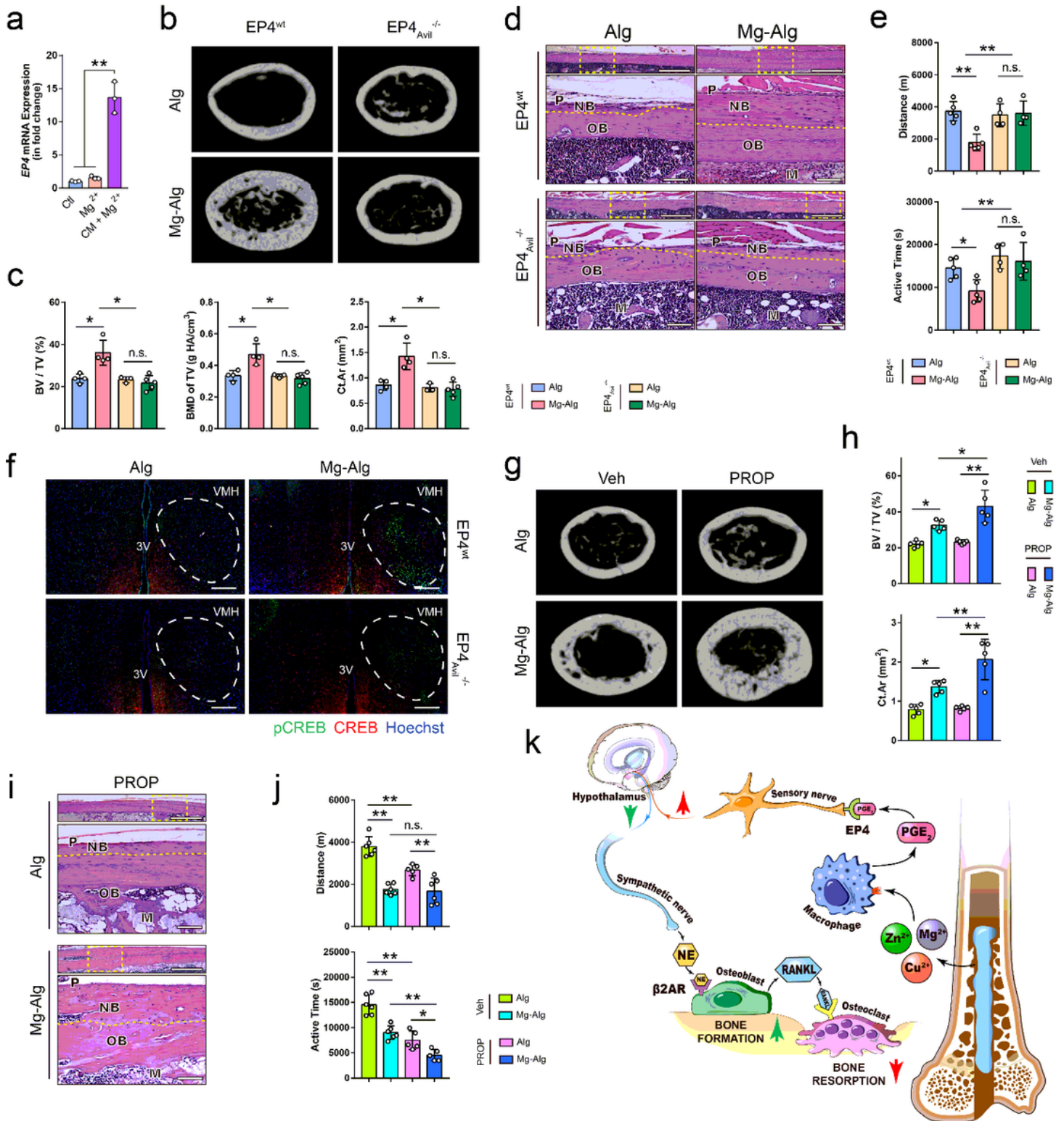


**Figure 6**

Knockout of PGE2 receptor 4 (EP4) in sensory nerves abolishes divalent cation-induced bone formation. (a) EP4 expression in DRG neurons stimulated by 10 mM Mg<sup>2+</sup> with or without the conditioned medium from Mg<sup>2+</sup>-treated macrophages. (b-d) Reconstructed  $\mu$ CT images (b), corresponding measurements (c), and representative H&E staining images (d) showing the new bone formation in EP4wt mice or EP4Avil<sup>-/-</sup> mice. Lower images are high-resolution versions (scale bars = 100  $\mu$ m) of the boxed regions in the

upper images (scale bars = 500  $\mu\text{m}$ ). (e) The running-wheel activity of EP4wt or EP4Avil<sup>-/-</sup> mice at week 4 postoperatively. (f) The phosphorylation of CREB in the VMH of EP4wt or EP4Avil<sup>-/-</sup> mice at week 1 postoperatively (scale bars = 200  $\mu\text{m}$ ). (g-i) Reconstructed  $\mu\text{CT}$  images (g), corresponding measurements (h), and representative H&E staining images (i) showing the new bone formation in mice injected with vehicle (Veh) or propranolol (PROP) Lower images (scale bars = 100  $\mu\text{m}$ ) are high-resolution versions of the boxed regions in the upper images (scale bars = 500  $\mu\text{m}$ ). (j) The running-wheel activity of mice injected with vehicle or propranolol at week 4 postoperatively. (k) Schematic diagram showing the findings of this study. The divalent cations triggered the production of PGE<sub>2</sub> from macrophages, which activated the EP4 at the sensory nerve to tune down sympathetic tones via the CREB signaling in the VMH, resulting in increased osteogenesis and decreased osteoclastogenesis in the periosteum. Data are mean  $\pm$  s.d. \*P<0.05, \*\*P<0.01 by 2-way ANOVA with Tukey's post hoc test (a, c, e, h, j).

## Supplementary Files

This is a list of supplementary files associated with this preprint. Click to download.

- [Supplementaryinformation.docx](#)